Available online at www.sciencedirect.com

jmr&t Journal of Materials Research and Technology

journal homepage: www.elsevier.com/locate/jmrt

Original Article

Numerical modeling and experimental validation of the effect of arc distribution on the as-solidified Ti64 ingot in vacuum arc remelting (VAR) process

E. Karimi-Sibaki [a], A. Kharicha [a,*], A. Vakhrushev [a], M. Abdi [a], M. Wu [b], A. Ludwig [b], J. Bohacek [c], B. Preiss [d]

[a] Christian-Doppler Laboratory for Metallurgical Applications of Magnetohydrodynamics, Montanuniversitaet of Leoben, Franz-Josef-Str. 18, A-8700 Leoben, Austria

[b] Chair of Simulation and Modeling of Metallurgical Processes, Montanuniversitaet of Leoben, Franz-Josef-Str. 18, A-8700 Leoben, Austria

[c] Heat Transfer and Fluid Flow Laboratory, Faculty of Mechanical Engineering, Brno University of Technology, Technicka 2896/2, 616 69 Brno, Czech Republic

[d] INTECO Melting and Casting Technologies GmbH, 8600 Bruck/Mur, Austria

ARTICLE INFO

Article history:
Received 21 March 2022
Accepted 7 May 2022
Available online 11 May 2022

Keywords:
Vacuum arc remelting (VAR)
Numerical modeling
Magnetohydrodynamics (MHD)
Axial magnetic field (AMF)
Melt pool profile
Ti64 alloy ingot

ABSTRACT

A numerical model coupling electromagnetic field and plasma arc impact with multiphase transport phenomena such as flow, heat transfer and solidification for the vacuum arc remelting (VAR) process is proposed. 3D simulations of the VAR process for refining a Titanium-based (Ti–6Al–4V) alloy are made. Different arc distributions (diffusive, constricted centric, constricted eccentric, and rotating arcs) under an axial magnetic field (AMF) are studied, focusing on their impact on the flow patterns and the resulting melt pool of the as-solidifying ingot. Simulation results show that diffusive arc leads to a shallow symmetrical melt pool; constricted centric and rotating arcs lead to electro-vortex flow and the symmetrical melt pool; constricted eccentric leads to electro-vortex flow as well, but the deepest non-symmetrical melt pool.

1. Introduction

Thermal energy is supplied through a DC arc to melt the tip of the electrode (impure alloy), aiming at producing ultra-clean alloys such as stainless steel, Nickel-based, and Titanium-based alloys in the vacuum arc remelting (VAR) process. The forming droplets at the tip of the melting electrode pass through the vacuum to reach the melt pool, which solidifies in a water-cooled mold to build the high-grade alloy ingot, as schematically shown in Fig. 1(a). Meanwhile, unfavorable elements with high vapor pressure like Pb, Sn, Bi, and Cu are evaporated under vacuum conditions. Low-density oxide

* Corresponding author.
E-mail address: Abdellah.kharicha@unileoben.ac.at (A. Kharicha).

https://doi.org/10.1016/j.jmrt.2022.05.036

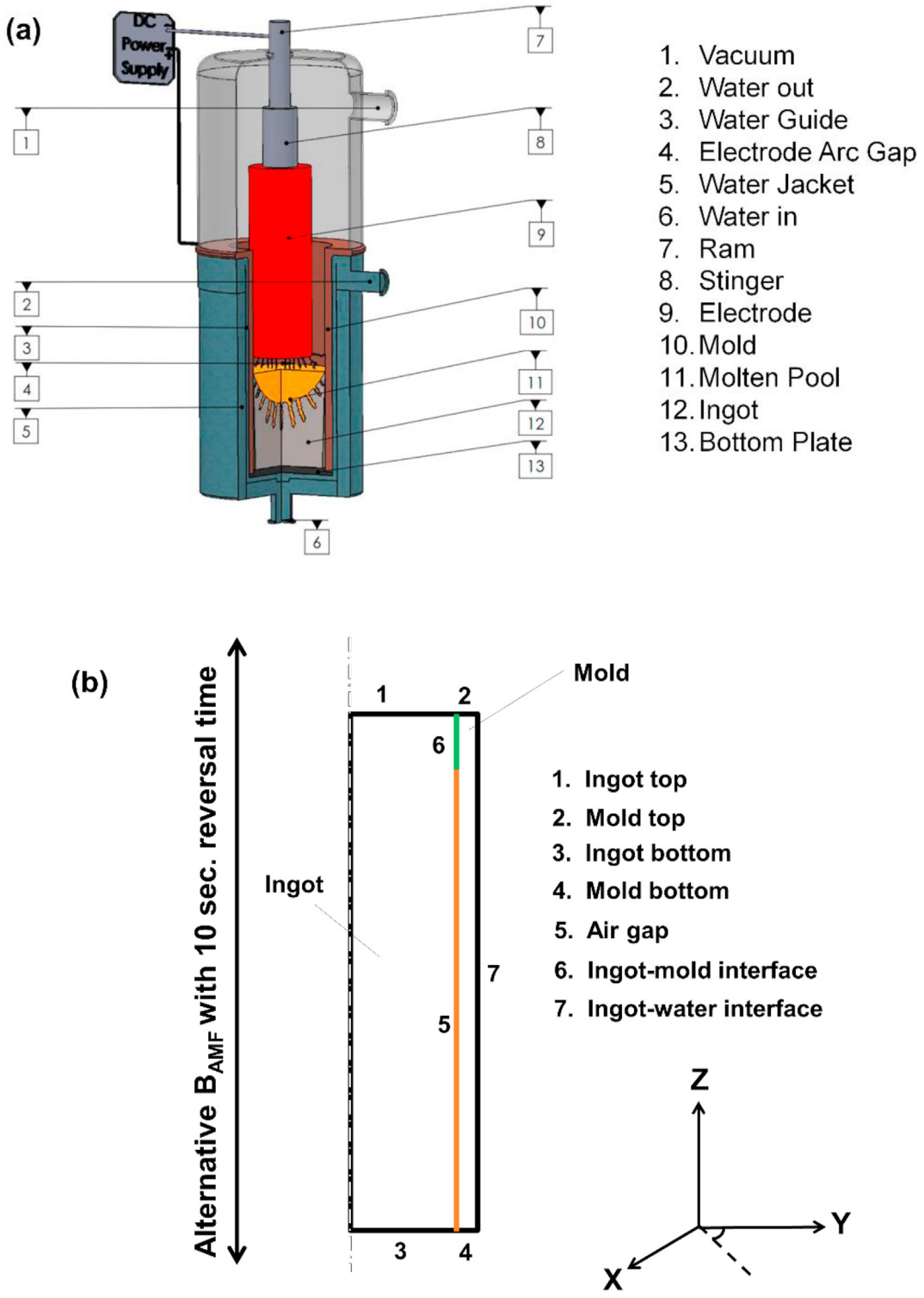

Fig. 1 – (a) Schematic representation of the VAR process; (b) A cross-section of the VAR process is shown to indicate different regions and boundaries.

inclusions as contaminants are transferred to the exterior surface of the ingot near the mold.

Most often, an external axial magnetic field (AMF) is deliberately introduced to stabilize the arc [1–6] that in turn can affect various phenomena in VAR, including the behavior of cathode spots emanating the plasma arc at the tip of the melting electrode [1,2,7,8], the distribution and movement of arc plasma [9–11], the thermal radiation in the vacuum [12], the solidification (macrosegregation and grain structure) of the ingot [13–21], and the interplay between the electromagnetic field and the flow as known as magnetohydrodynamics (MHD) in the melt pool [19–22].

The flow greatly influences the thermal field and solidification of the ingot in the melt pool of VAR. The latter is governed by thermosolutal buoyancy and Lorentz force, which arises from the interaction between the electric current density and both self-induced, axial magnetic fields (AMF) [23]. The self-induced magnetic field (dominantly in the azimuthal direction) is originated in the imposed electric current flowing through the entire system. The electric current density field on the top of the ingot and consequently within the melt pool is governed by the arc distribution in the vacuum region.

From a modeling point of view, mainly aiming to study MHD in the melt pool and solidification of the ingot using axisymmetric assumption, it is convenient/sufficient to define the arc distribution at ingot top customarily using a Gaussian distribution [17,20,24–26]. For that purpose, a parameter, namely arc radius (fraction of ingot radius), is introduced [17,20,24–26]. A low arc radius represents a constricted, whereas a high arc radius indicates a diffusive arc. Such an approach is adequate when the arc remains centric during the entire operation of VAR. Herein, we extend this scheme to include other frequently in-situ observed arcs during VAR [27–29]. Thus, we put forward four types of arcs, including diffusive, constricted centric, constricted eccentric, and constricted rotating arc.

In the present study, we perform a comprehensive investigation on the impact of the aforementioned arc types under an axial magnetic field (AMF) on transport phenomena in a VAR process of a titanium-based (Ti–6Al–4V) alloy. The electromagnetic and thermal fields are computed in the mold and ingot. Additionally, influences of flow patterns arising from different arc types on the solidification of the ingot are thoroughly analyzed. Ultimately, the obtained numerical results can help engineers improve the design and operational parameters of the VAR process.

2. Modeling

All governing equations and boundary conditions related to flow, electromagnetic, and thermal/solidification fields are discretized considering the Finite Volume Method (FVM). Several User-defined functions (UDF) [30] are implemented in the commercial CFD software, ANSYS FLUENT v.17.1, to account for special boundary conditions and modeling equations related to the MHD in the melt pool, arc, solidification, etc.

For the sake of simplicity and to avoid extra complexity, the following assumptions are made for all simulations:

(i) The ingot top, which is in direct contact with the plasma arc, is assumed to be stationary and flat. To implicitly account for the impact of arc, a Gaussian distribution of electric current density on the ingot top is assumed [20,24–26]. Details will be further elucidated after introducing governing equations.

(ii) The electrode, mold, ingot, and arc participate in a complex radiative heat exchange within the vacuum region [12,31]. Considering the small difference between the electrode and ingot diameters in VAR, a simplified approach assuming the well-known Stefan–Boltzmann law with an emissivity coefficient of 0.9 is used to determine the radiation heat transfer rate from the electrode tip to the ingot top. Whilst the temperature field at the ingot top is computed, the experimental measurement of the temperature of the electrode tip during the operation is utilized. The latter is reported to be ca. 150 K above the liquidus of the alloy [7].

(iii) The formation of droplets at the electrode tip and their dripping in the vacuum zone are not tracked. Droplets convey mass, energy, and momentum to the melt pool. Thus, source terms are introduced to governing equations of continuity, momentum, and energy to implicitly take into account the impact of droplets on transport phenomena in the melt pool. Derivations and formulas of those source terms are extensively described in Ref. [32].

(iv) At the top edge of the ingot adjacent to the mold, where the as-solidified shell is still "soft", or the alloy is liquid, a pre-defined contact (20 mm) is assumed. Below the contact zone, the ingot shrinks away from the mold to form an air gap, as shown in Fig. 1(b).

2.1. Governing equations

The A-φ method is used to compute the electromagnetic field [33,34], where A is magnetic vector potential, and φ denotes electric scalar potential. Electric potential is calculated through the conservation equation of electric current density ($\nabla\cdot\vec{j}=0$). The current density includes two parts as follows:

$$\vec{j}=-\sigma\nabla\phi-\sigma\frac{\partial\vec{A}}{\partial t}. \tag{1}$$

The electric conductivity (σ) and magnetic permeability (μ_0) of metals are needed to calculate magnetic field ($\vec{B}=\nabla\times\vec{A}$) through,

$$\vec{j}=\nabla\times\left(\frac{1}{\mu_0}\nabla\times\vec{A}\right)-\nabla\left(\frac{\lambda_p}{\mu_0}\nabla\cdot\vec{A}\right) \tag{2}$$

To ensure a unique solution to Eq. (2), the Coulomb gauge ($\nabla\cdot\vec{A}=0$) is satisfied [33]. Additionally, a penalty function term (λ_p) between zero and one in an ad-hoc way is introduced to enforce zero divergence of the magnetic field [32,35,36]. Eventually, the calculated Lorentz force ($\vec{F}_L=\vec{j}\times\vec{B}$) is added as momentum source term for the flow calculation.

An enclosed region with a diameter of three times larger than that of the mold is considered where all magnetic vector potential components (axial, radial, and tangential) are set to zero. Continuity of magnetic potential is considered at all interior boundaries [35,36]. The air gap is electrically insulating. Thereby a zero flux of electric potential is used. The magnitude of electric potential at the mold top is zero. The electric current density (flux of electric potential) at the ingot top is assumed to follow a Gaussian distribution ($j_{ingot-top}=\frac{I_0\exp\left(-\frac{r^2}{R_a^2}\right)}{\int_0^{R_i}2\pi r\exp\left(-\frac{r^2}{R_a^2}\right)dr}$) as described in assumption (i). I_0, R_i, and R_a are the magnitude of imposed current, ingot radius, and arc radius respectively. Conventionally, the arc radius is

defined as a fraction of the ingot radius [20,24–26]. The peak of current density is located at the central axis of the ingot for both the diffusive arc ($R_a = 0.7R_i$) and constricted centric arc ($R_a = 0.2R_i$). However, the distance of the peak value of constricted eccentric arc ($R_a = 0.2R_i$) and rotating arc ($R_a = 0.2R_i$) from the central axis is tantamount to the mid-radius of the electrode [27–29]. Experimental measurements revealed that the time period of a single rotation around the center is in the range of one to 20 s for the rotating arc [27–29]. In the present study, we simulate the rotating arc considering 20 s for the time period for rotational motion.

The flow field is calculated considering continuity, Eq. (3), and momentum, Eq. (4), conservations as follows:

$$\frac{\partial \rho}{\partial t} + \nabla \cdot (\rho \vec{u}) = 0 \tag{3}$$

$$\frac{\partial}{\partial t}(\rho \vec{u}) + \nabla \cdot (\rho \vec{u}\vec{u}) = -\nabla p + \nabla \cdot \left(\mu_{eff}(\nabla \vec{u} + \nabla \vec{u}^{T})\right) + \rho_0 \vec{g}\beta(T - T_0) + \vec{F}_L + \vec{F}_P \tag{4}$$

μ_{eff} denotes the effective viscosity including turbulence; p is the pressure; $\vec{g}$ is the gravity constant; β is the thermal expansion coefficient; ρ_0 and T_0 are reference density and reference temperature respectively to calculate thermal buoyancy according to Boussinesq approximation; $\vec{F}_L$ and $\vec{F}_P$ are Lorentz and interdendritic drag forces respectively. The latter appears inside the mushy zone of solidifying ingot, and it is determined through the isotropic model of Kozeny-Carman [24,26,37,38],

$$\vec{F}_P = -\frac{A_{mush}(1-f)^2}{f^3}(\vec{u} - u_s). \tag{5}$$

A large value (e.g. 10^8) for mushy zone constant (A_{mush}) ensures smooth suppression of flow within the mushy zone; u_s denotes the casting speed; f is liquid volume fraction which is linearly correlated to temperature (T), alloy liquidus temperature (T_{Liq}) and alloy solidus temperature (T_{Sol}) [17–22,25,26,37],

$$f = \min\left\{1,\ \max\left\{0, \frac{T - T_{Sol}}{T_{Liq} - T_{Sol}}\right\}\right\}. \tag{6}$$

The non-slip boundary condition is considered at the ingot-mod interface and air gap boundaries, whereas the ingot top condition is free-slip. In addition, the casting speed (u_s) is specified at the ingot bottom.

The thermal field is calculated through the enthalpy (h) conservation equation:

$$\frac{\partial}{\partial t}(\rho h) + \nabla \cdot (\rho \vec{u} h) = \nabla \cdot (\lambda_{eff} \nabla T) + S. \tag{7}$$

λ_{eff} denotes effective thermal conductivity, including the effect of turbulence, and the source term ($S = -\frac{\partial}{\partial t}(\rho L f) - L u_s \nabla f$) describes the impact of solidification latent heat where L is the latent heat of fusion of alloy.

The thermal boundary condition at the ingot top is modeled considering radiative heat exchange as thoroughly described in assumption (ii). Heat transfer coefficient of 500 $\frac{W}{m^2K}$ is specified for the contact area at the ingot-mold interface and ingot bottom [39,40], whereas the heat transfer coefficient of 7000 $\frac{W}{m^2K}$ is prescribed at mold-water interface [20,26,32,41]. The air gap is a conjugate wall where radiation heat transfer from the ingot to the mold is considered to complete all necessary boundary conditions for the thermal field in the entire system [20,39,41].

The Scale-Adaptive Simulation (SAS) model is utilized to account for the turbulence in the melt pool [42,43]. SAS is insensitive to the grid spacing of the near wall cells, effective, and fairly as accurate as of the LES model with lower computational cost [42,43]. Many researchers extensively used two-equation models of turbulence such as SAS to calculate turbulent flow in metallurgical and remelting processes [19–22,24–26,32,44,45].

2.2. Other settings

A very fine mesh is generated for simulation activities involving a total number of ca. 0.6 million mesh elements for the full 3D calculation to accurately predict transport phenomena. Transient calculations are performed. The pool profile becomes firmly steady after sufficient calculation time despite the transient nature of field structures such as velocity, thermal, and electromagnetic fields. This implies that the process reaches a quasi-steady state. As the turbulent flow is spatially disordered in the melt pool, a statistical analysis of the flow is carried out to characterize the transient behavior of the flow and to determine the quasi-steady state results. Details will be further described in the section "4. Discussions".

An experimental investigation was conducted by Hosamani et al. [46] to study the effect of an axial magnetic field (AMF) on the solidification behavior of a Titanium-based (Ti–6Al–4V) alloy ingot produced through vacuum arc remelting (VAR) process. Herein, their experimental setup is used to configure our numerical model. Geometrical data and operational parameters of the process are listed in Table 1. For our simulations, all required material properties of Ti–6Al–4V alloy (e.g. heat capacity, thermal conductivity, etc.) that are mostly temperature-dependent are extracted from Refs. [47–50]. A summary of the properties is available in Ref. [51].

3. Results

In the present study, the VAR process operates under a time-varying axial magnetic field (AMF) with a reversal time of 10 s for the direction of the magnetic field. In other words, the direction of AMF is upward in the first 10 s, whereas the

Table 1 – Operating conditions of the VAR process (Ref. [46]) used in our calculations.

Operation parameters	
Ingot diameter (mm)	165
Electrode diameter (mm)	114
Mold length (mm)	800
Ingot length (mm)	545
Melt rate (kg/hr)	58.8
Gap length (mm)	15
DC current (kA)	2.5
B_{AMF} (G)	45
Reversal time (s)	10

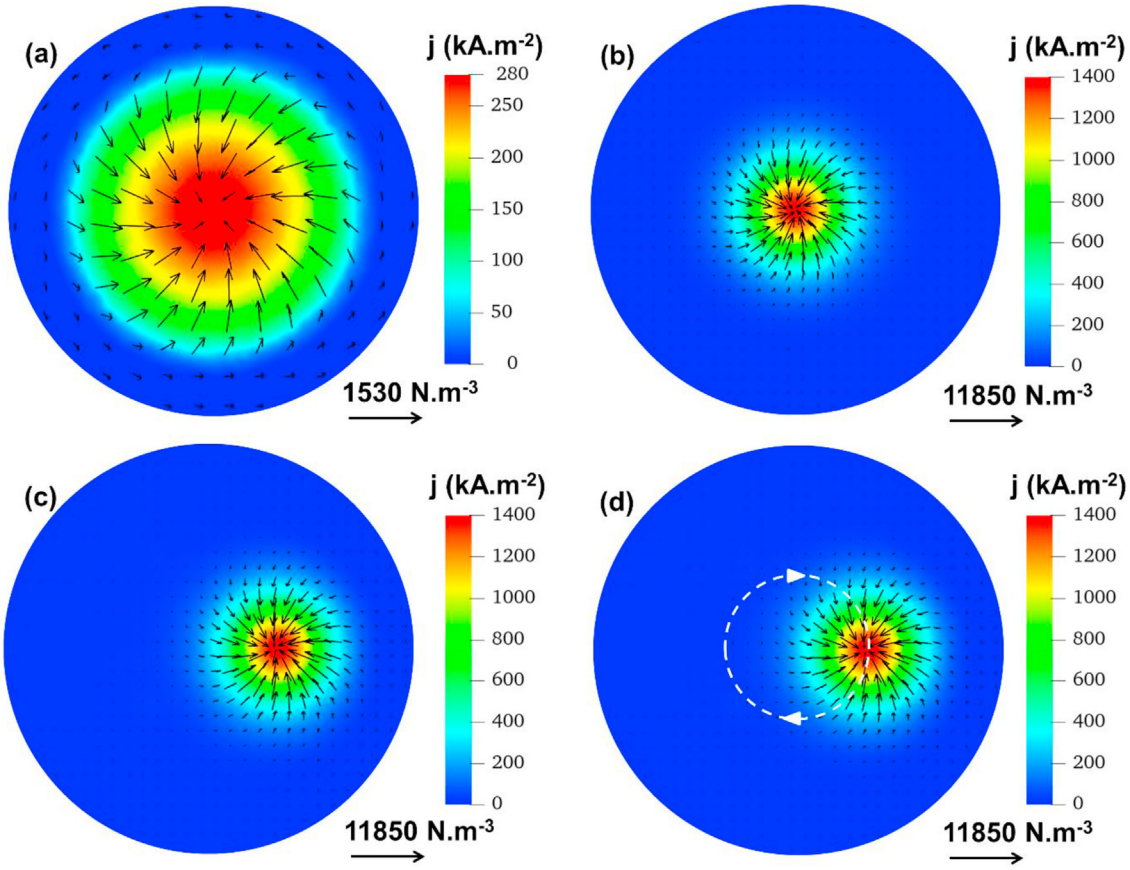

Fig. 2 – Electric current density (contour) and Lorentz Force (vector) fields at ingot top: (a) diffusive; (b) constricted centric; (c) constricted eccentric; (d) rotating arcs.

direction is downward in the next 10 s. This cycle continues during the whole operation of the process [46]. Herein, different scenarios regarding the distribution of arc on the ingot top surface such as diffusive, constricted centric, constricted eccentric, and rotating arcs are investigated. The global distribution of electric current density within the VAR process is well-known [20,25,26]. A fraction of electric current flows through the contact area at the ingot-mold interface, and part of the current directly travels toward the ingot bottom [20]. The arc delivers the electric current to the ingot top surface. Thus, the electric current density distribution at the ingot top significantly influences the magnetic field and, consequently, the distribution of Lorentz force, as shown in Fig. 2. As pointed out in "2. Modeling", a Gaussian distribution of electric current density for the diffusive arc ($R_a = 0.7R_i$), Fig. 2(a), constricted centric arc ($R_a = 0.2R_i$), Fig. 2(b), constricted eccentric arc ($R_a = 0.2R_i$), Fig. 2(c), and rotating arc ($R_a = 0.2R_i$), Fig. 2(d), is considered. The distance of the peak value of constricted eccentric and rotating arcs from the central axis is equivalent to the mid-radius of the electrode [27–29]. The intensity of the electric current increases as the radius of the arc decreases. As a consequence, strong local Lorentz force is predicted for centric, eccentric, and rotating arcs. In contrast, the force distributes in a relatively smooth way from the center of the ingot toward the mold, as shown in Fig. 2. In all cases, the force converges inwardly toward the center of the arc, where the peak value of electric current density exists. Additionally, the entire force field slightly rotates in the counterclockwise direction. Of note, the field switches to rotate clock wisely as the direction of AMF changes from upward to downward. To simulate the rotating arc, we simply require to rotate the calculated Lorentz force vector field considering eccentric arc in the entire domain about the central axis of ingot (z-direction) as shown in Fig. 2(d). As anticipated, the arc distribution can remarkably influence MHD and heat transfer in the melt pool. To effectively demonstrate field structures like flow or thermal fields using images due to the transient character of AMF. Therefore, transient results are shown through animations in supplemental materials including "Diffusive_Arc.avi", "Centric_Arc.avi", "Eccentric_Arc.avi", and "Rotating_Arc.avi". Readers are highly encouraged to observe those animations. In the following, we illustrate a few snapshots at different times of field structures for all arc types aiming at exploring the interplay between various transport phenomena within VAR. Unlike the animations, the computational domain is shown partially (only top ingot near melt pool) in all figures to illustrate concisely but more concretely the field structures presented in this paper.

Considering the diffusive arc, snapshots at different times for variations of thermal and velocity (magnitude and direction) fields starting sometime (t_0) in the middle of the process

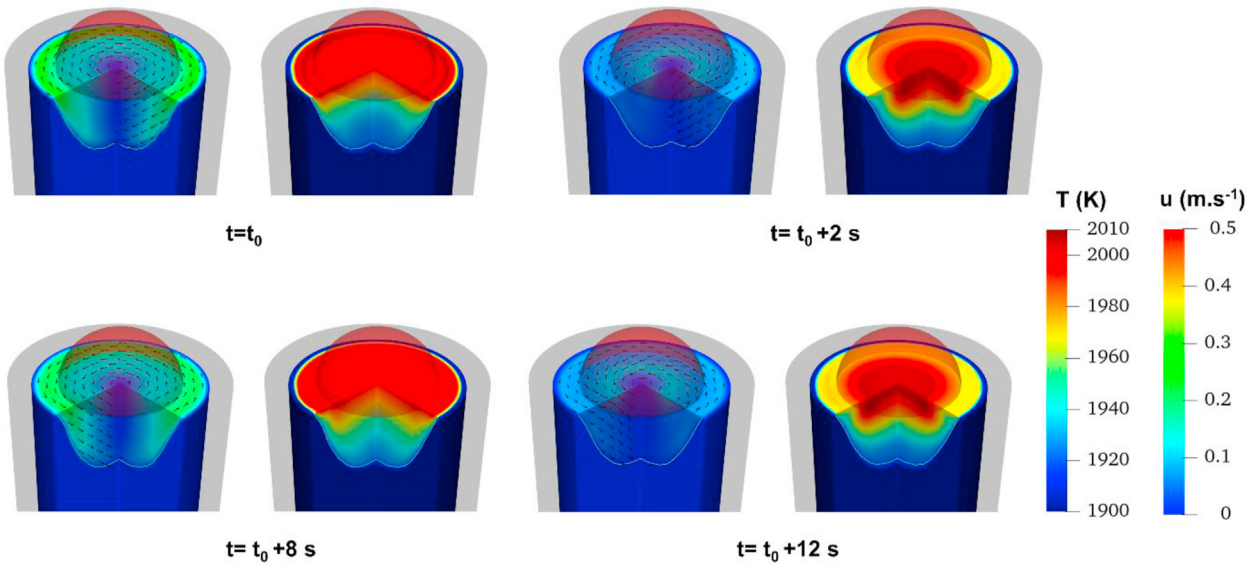

Fig. 3 – Snapshots at different times of velocity and thermal fields in the melt pool starting sometime (t_0) in the middle of the process are shown. The transparent semi-sphere illustrates the diffusive arc.

are illustrated in Fig. 3. At this moment, the direction of AMF switches to become upward. Consequently, the developed flow which rotates clock wisely slows down. Shortly afterwards, the velocity in the axial direction increases that in turn enhancing advection of the hot melt from the ingot top near the center of the arc to the bulk of the melt pool, as shown at the time (t_0 +2 s). As time proceeds, the strong toroidal flow in the counterclockwise develops once again as indicated at time (t_0 +8 s). Accordingly, the stirring of melt is promoted, and the thermal field becomes relatively uniform. The direction of AMF alters at the time (t_0 +10 s) to become downward; hence the toroidal flow slows down as shown at the time (t_0 +12 s). Soon after, the toroidal flow, which rotates clock wisely, develops that was described/shown for the time (t_0). This cycle continues during the entire operation of the process. Details regarding time evolution of velocity and thermal fields within the bulk of melt pool and ingot top are illustrated in the animation "Diffusive_Arc.avi".

Considering the constricted centric arc, snapshots at different times for variations of thermal and velocity fields start sometime (t_0) in the middle of the process are shown in Fig. 4. The overall behavior of the process is similar to that of the diffusive arc. In essence, the toroidal flow slows down and changes its direction as the direction of AMF switches. Meanwhile, the axial flow in the bulk of melt under the shadow of the constricted centric arc intensifies. Thereby, the

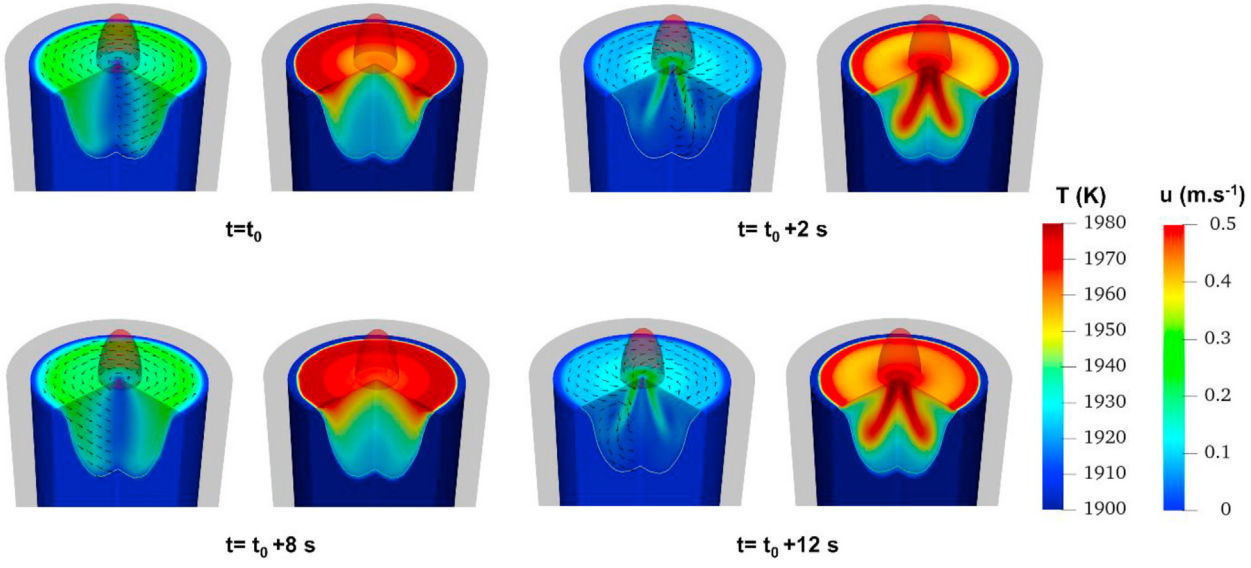

Fig. 4 – Snapshots at different times of velocity and thermal fields in the melt pool starting sometime (t_0) in the middle of the process are shown. The transparent blunt cone illustrates the constricted centric arc.

hot melt is advected from the ingot top to the bulk of the melt pool. Lorentz force (Fig. 2) and consequently central axial velocity for the constricted centric arc is stronger than that of diffusive arc. Thus, the hot melt can travel a longer distance to deepen the melt pool in the case of a constricted centric arc compared to a diffusive arc. Details regarding time evolution of velocity and thermal fields inside the bulk of melt pool and ingot top for constricted centric arc are illustrated in the animation "Centric_Arc.avi".

Considering the constricted eccentric arc, snapshots at different times for variations of thermal and velocity fields start sometime (t_0) in the middle of the process are illustrated in Fig. 5. Here, the transient flow field under AMF closely resembles the flow pattern of a centric arc. Thus, a strong electro-vortex flow develops. However, the peak value is off-center, leading to a non-symmetrical pool profile. Shortly after the alteration of the direction of AMF and deceleration of the clock wisely rotating flow at the time (t_0 +2 s), the constricted eccentric arc enforces the liquid melt to flow vertically near the mold. Consequently, a non-uniform thermal field and a non-symmetrical pool profile develop. Details regarding the time evolution of velocity and thermal fields inside the bulk of melt pool and ingot top for constricted eccentric arc are illustrated in the animation "Eccentric_Arc.avi".

Snapshots at different times for the rotating arc are illustrated in Fig. 6. The arc rotates clock wisely, considering 20 s for the time period for rotational motion. Herein, both the alteration of the direction of AMF and the rotation of arc can influence the flow in the azimuthal direction. A complex flow pattern is predicted. Regardless of the location of the arc, an axial flow under the shadow of the arc is observed. Far away from the arc, the azimuthal flow (clockwise/counter-clockwise) is governed by the direction of AMF (downward/upward), similar to what was previously described for other types of arc. The thermal field becomes relatively uniform in the melt due to rigorous mixing. Unlike the aforementioned thermal fields for other arcs, the hottest region of the melt pool is not located under the shadow of the rotating arc. Indeed, the hot melt on the ingot top is advected by the 3D chaotic flow in the melt pool, which is thoroughly demonstrated in the animation "Rotating_Arc.avi".

4. Discussions

The flow in the melt pool is transient, chaotic, and spatially disordered. A convenient way of characterizing the instantaneous velocity field in such transient flow is utilizing statistical parameters such as the mean velocity and the variance. The former enables us to identify the average velocity, and the latter helps us to extract velocity fluctuations everywhere inside the melt pool.

Mean velocity components in all directions ($\overline{u}_x$, $\overline{u}_y$, and $\overline{u}_z$) are extracted to compute the average speed in the melt pool, $\|u\| = \sqrt{\overline{u}_x{}^2 + \overline{u}_y{}^2 + \overline{u}_z{}^2}$, as well as the variance of velocity components in all directions ($s_i^2 = \frac{1}{N}\sum_{n=1}^{N}(u_i - \overline{u}_i)^2, \quad i = x, y, z.$) during transient simulations. Calculations were carried out over a long period of physical process time (~50 min) with ca. 50,000 total number of samples (N) to achieve statistical invariance.

The results of our analysis are illustrated in Fig. 7 and Fig. 8. The mean velocity field is predicted to be minimal without any specific flow pattern considering the diffusive arc, as shown in Fig. 7(a). The well-known electro-vortex flow develops with the peak value under the arc shadow for the constricted centric arc, as shown in Fig. 7(b). An intense electro-vortex flow with the peak value situated away from the center axis is predicted for the constricted eccentric arc, as shown in Fig. 7(c). The rotational motion of the arc can significantly influence the mean velocity field, as indicated in Fig. 7(d). The peak value of mean velocity is located on the rotational path of the arc.

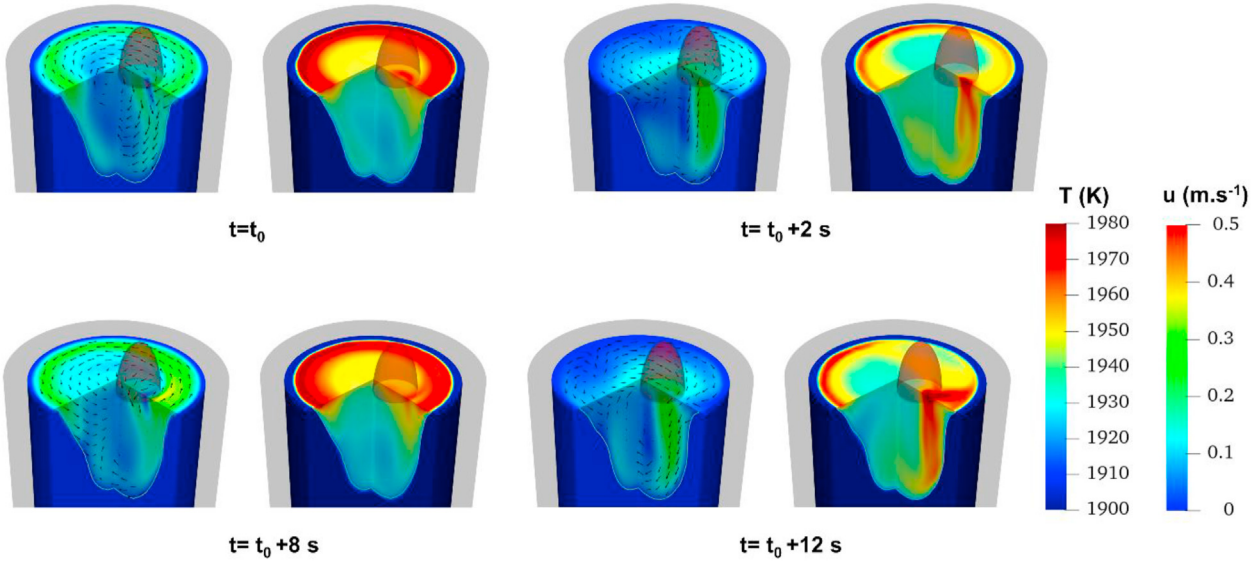

Fig. 5 – Snapshots at different times of velocity and thermal fields in the melt pool starting sometime (t_0) in the middle of the process are shown. The transparent blunt cone illustrates the constricted eccentric arc.

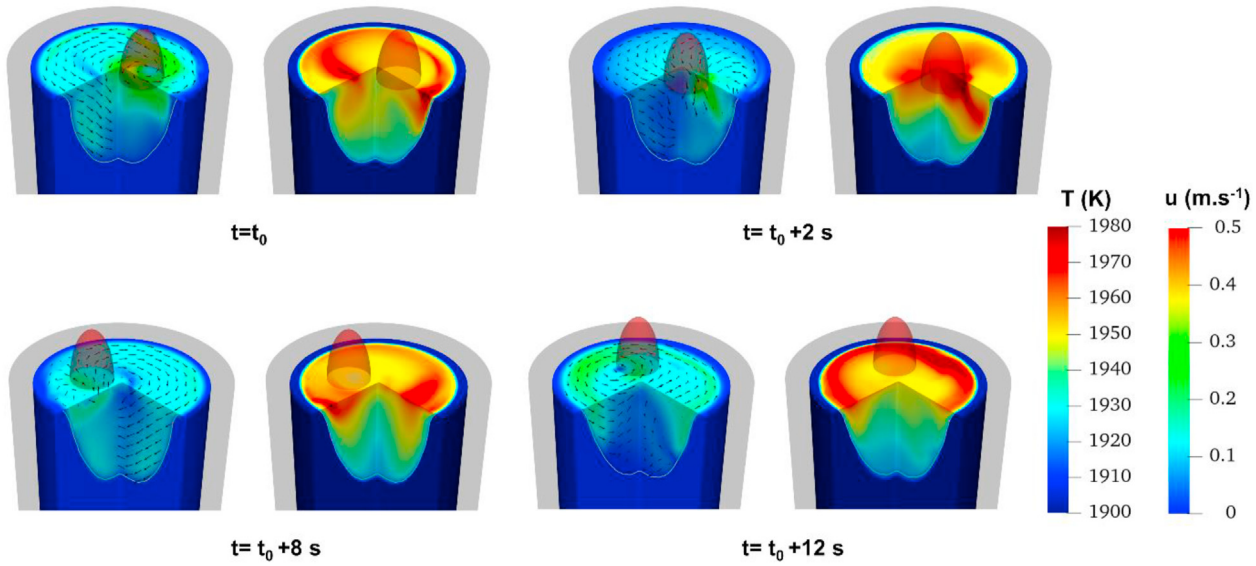

Fig. 6 – Snapshots at different times of velocity and thermal fields in the melt pool starting sometime (t_0) in the middle of the process are shown. The transparent blunt cone illustrates the rotating arc.

The calculated variance indicating fluctuations of the velocity field is shown in Fig. 8. Notable fluctuations in the same area near the ingot-mold interface and under the shadow of the arc were predicted for constricted centric/eccentric arcs. The diffusive arc did not exhibit a substantial fluctuation near the center of the axis as the arc, and consequently, Lorentz force (Fig. 2) was smoothly distributed around the ingot top. In contrast, the peak value of fluctuation is adjacent to the center of the ingot (also the axis of the rotational path), as shown in Fig. 8(d) for the rotating arc. Also, considerable fluctuations along the path of rotation were observed. For all varieties of arcs, the flow remains almost statistically invariant (slight fluctuations) deep into the melt pool.

Despite transient flow in the melt pool, the pool profile reaches a quasi-steady state. Conventionally, the pool profile is an indicator of the internal quality of the ingot

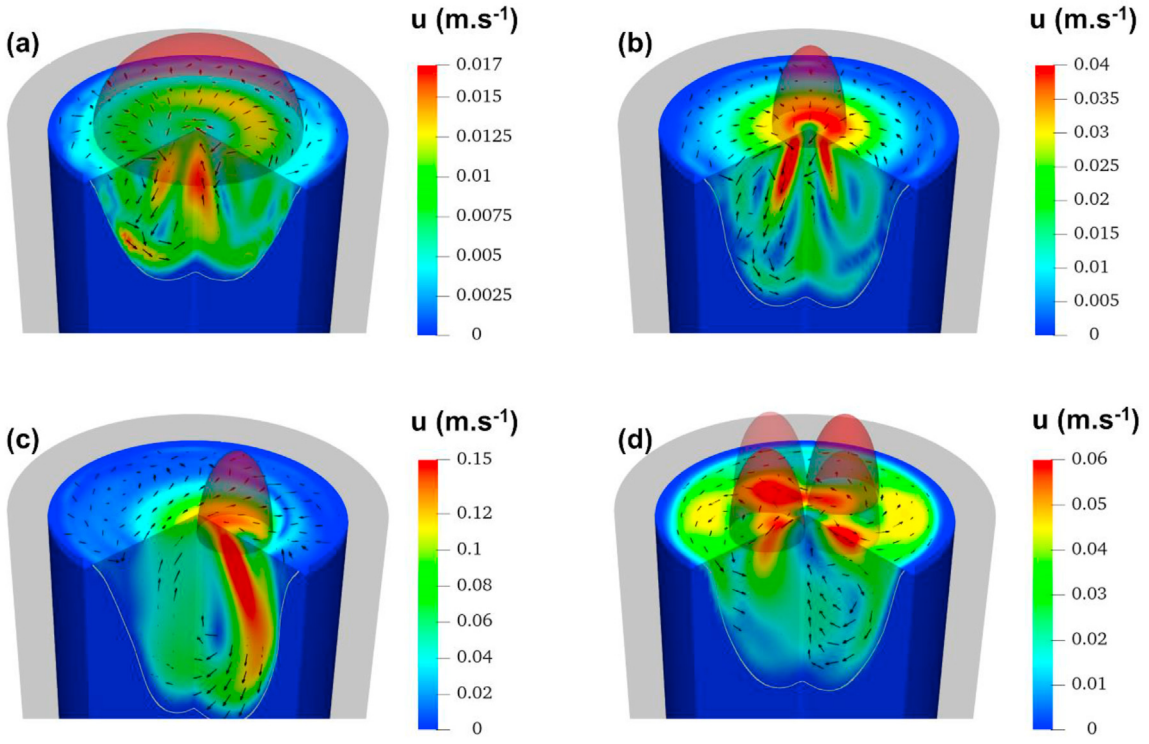

Fig. 7 – Calculated mean velocity field in the melt pool: (a) diffusive arc; (b) constricted centric arc; (c) constricted eccentric arc; (d) rotating arc.

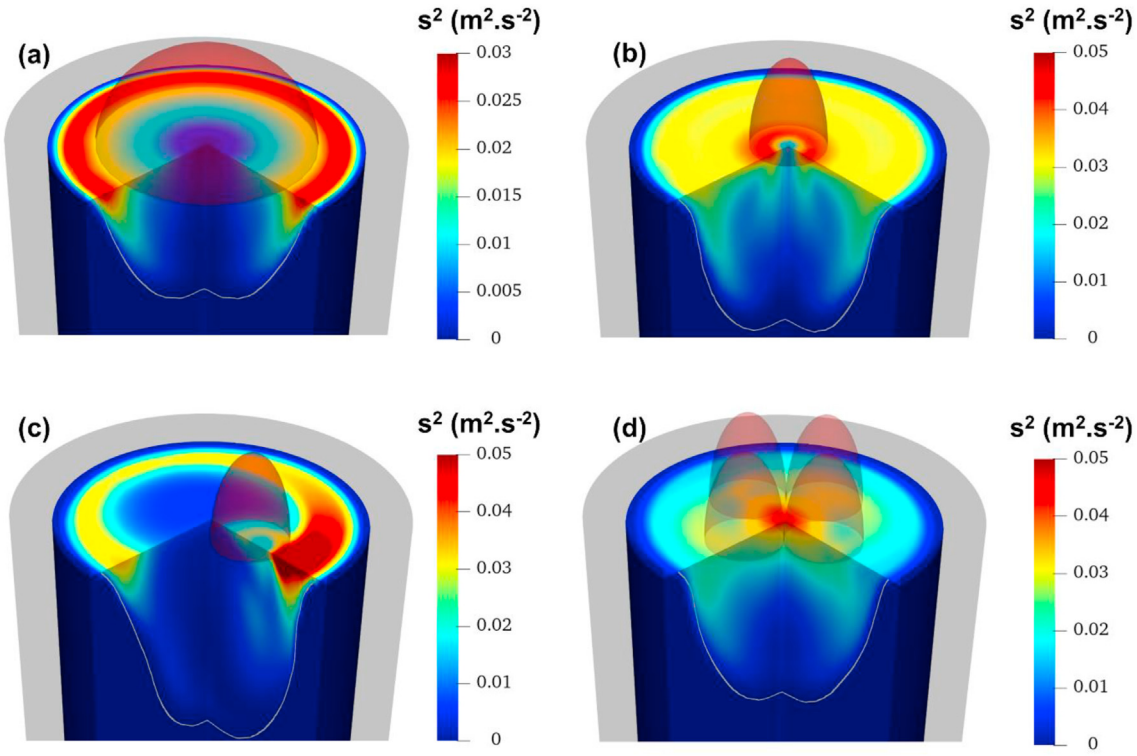

Fig. 8 – Calculated variance of velocity field in the melt pool: (a) diffusive arc; (b) constricted centric arc; (c) constricted eccentric arc; (d) rotating arc.

[20,25,26,32,46]. A shallow and symmetrical melt pool promotes unidirectional solidification and consequently the formation of a segregation-minimal alloy ingot. The predicted pool profiles concerning different types of arcs are compared with the experiment [46] in which Nickel particles were used to mark the pool profile. Several cross-section cuts revolving 45° perpendicular to the ingot top and through the center axis of the ingot are made to view the calculated pool profile. A summary of the results is illustrated in Fig. 9.

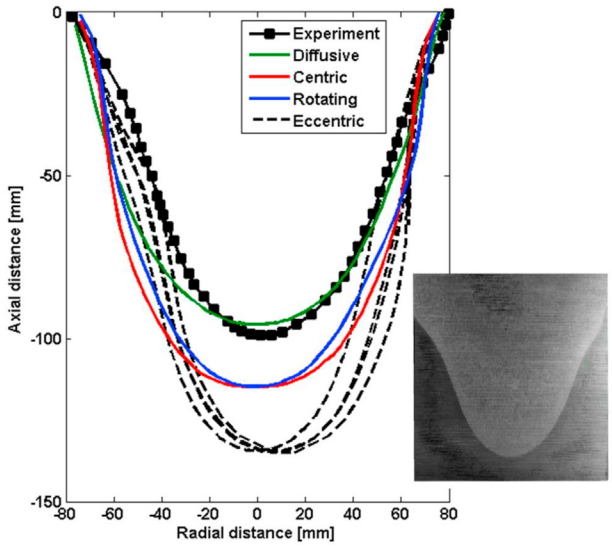

Fig. 9 – A comparison is made between the calculated pool profile extracted from several cross-section cuts of ingot considering varieties of arc and the experimentally marked pool profile extracted from Ref. [46]. Reference [46] is available under Creative Commons By Attribution 4.0 in: https://creativecommons.org/licenses/by/4.0/.

The process operating under diffusive, constricted centric, and rotating arcs produce a symmetrical pool as all profiles extracted from different cross-section cuts completely overlap, as shown in Fig. 9. However, the constricted eccentric arc promotes the formation of a deep non-symmetrical pool profile, as indicated in Fig. 9. Thus, the radius and location of the arc significantly impact the pool profile and consequently the internal quality of the ingot. Based on the aforementioned desired pool profile characteristics (e.g. shape and depth), the highest quality of the ingot is achieved under a diffusive arc, whereas the worst quality of the ingot is obtained under a constricted eccentric arc.

Considering the experimental pool profile, as shown in Fig. 9, a longitudinal section was taken from the central portion of the ingot to reveal the melt pool profile. Apparently, the pool profile is not perfectly symmetrical. A reasonable agreement is observed between numerical results, especially for the diffusive arc and the experiment in the central part of the ingot. However, a discrepancy between those results arises near the mold wall where a better match between the experiment and the result through the eccentric arc is achieved. This implies that a combination of those arc types may occur during the VAR operation. This study aids the industry to understand the importance of arc control during VAR. By

analyzing an industry ingot with a marked pool shape, compared to the simulation results, one can infer the possible cause of arc eccentricity.

5. Summary

Several 3D simulations were performed to analyze the interaction between field structures such as thermal, magnetic and flow fields in the vacuum arc remelting (VAR) process. We classified four arc types: diffusive, constricted centric, constricted eccentric, and rotating arcs. The influences of arc types under an axial magnetic field (AMF) on the field structures and the quality of the final ingot considering pool profile were examined. The main conclusions are as follows:

- The turbulent flow field is statistically analyzed. No specific flow pattern was predicted considering diffusive arc, whereas electro-vortex flow was observed considering constricted centric, constricted eccentric, and rotating arcs.
- The peak velocity is observed under the shadow of the arc or the rotational path of the arc. Considerable velocity fluctuations about the mean value were detected under arc shadow and near the ingot-mold interface.
- A symmetrical pool profile as an indicator of the internal quality of the ingot was predicted considering diffusive, constricted centric, and rotating arcs.
- The longest depth of pool for constricted eccentric arc, and the shortest depth for diffusive arc were observed. Also, the constricted eccentric arc results in a non-symmetrical pool profile.

Numerical results are validated against an experiment to correlate the arc type with the pool profile of the melt. A combination of all arc types may exist during a single operation of the VAR process that can prevent the formation of a perfectly symmetrical pool profile. All transient results are shown through animations in supplementary data.

Declaration of Competing Interest

We have no conflicts of interest to disclose.

Acknowledgements

The authors acknowledge financial support from the Austrian Federal Ministry of Economy, Family and Youth and the National Foundation for Research, Technology and Development within the framework of the Christian-Doppler Laboratory for Metallurgical Applications of Magnetohydrodynamics.

Appendix A. Supplementary data

Supplementary data to this article can be found online at https://doi.org/10.1016/j.jmrt.2022.05.036.

REFERENCES

[1] Anders A. Cathodic arcs from fractal spots to energetic condensation. Berkeley, CA USA: Springer; 2008. New York, NY.
[2] Montcel BT, Chapelle P, Creusot C, Jardy A. IEEE Trans Plasma Sci 2018:1–9.
[3] Wang L, Jia S, Shi Z, Rong M. J Appl Phys 2006;100(11). article 113304.
[4] Langlois Y, Chapelle P, Jardy A, gentils F. In: Int. Symp. On discharges and electrical insulation in vacuum; 2010.
[5] Delzant P-O, Chapelle P, Jardy A, Jourdan J, Jourdan J, Millet Y. Proc Liq Met Process Cast Conf 2017:9–14.
[6] Nair BG, Jourdan J, Millet Y, Ward RM. Proc Liq Met Process Cast Conf 2017:15–20.
[7] Zanner FJ, Bertram LA, Adasczik C, O'Brien T. Metall Trans A B 1984;15(1):117–25.
[8] Chapelle P, Noël C, Risacher A, Jourdan J, Jardy A, Jourdan J. J Mater Process Technol 2014;214(11):2268–75.
[9] Zanner FJ, Bertram LA, Harrison R, Flanders HD. Metall Trans A B 1986;17(2):357–65.
[10] Woodside RC, King PE. Int Symp Liq Met Process Cast 2009:75–84.
[11] Risacher A, Chapelle P, Jardy A, Escaffre J, Poisson H. J Mater Proc Technol 2013;213(2):291–9.
[12] Zagrebelnyy D, Krane MJM. Metall Mater Trans B 2009;40(3):281–8.
[13] Watt T, Taleff E, Lopez F, Beaman JJ, Williamson RL. Int Symp Liq Met Process Cast 2013:261–70.
[14] Xu X, Zhang W, Lee PD. Metall Mater Trans A 2002;33(6):1805–15.
[15] Revil-Baudard M, Jardy A, Combeau H, Leclerc F, Rebeyrolle V. Metall Mater Trans B 2014;45(1):51–7.
[16] Schlatter R. J Vac Sci Technol 1974;11:1047–54.
[17] Patel A, Fiore D. IOP Conf Ser Mater Sci Eng 2016;143. article 12017.
[18] Hans S, Ryberon S, Poisson H, Heritier P. Int Symp Liq Met Process Cast 2013.
[19] Kou H, Zhang Y, Yang Z, Li P, Li J, Zhou L. Int J Eng Technol 2012;12:50–6.
[20] Karimi-Sibaki E, Kharicha A, Wu M, Ludwig A, Bohacek J. Metall Mater Trans B 2021;52:3354–62. https://doi.org/10.1007/s11663-021-02264-w.
[21] Shevchenko DM, Ward RM. Metall Mater Trans B 2009;40(3):248–53.
[22] Jardy A, Ablitzer D. Mater Sci Technol 2009;25(2):163–9.
[23] Davidson PA, He X, Lowe AJ. Mat Sci Tech 2000;16:699–711.
[24] Pericleous K, Djambazov G, Ward M, Yuan L, Lee PD. Metall Mater Trans A 2013;44(12):5365–76.
[25] K.M. Kelkar, S.V. Patankar, A. Mitchell, O. Kanou, N. Fukada, and K. Suzuki: https://inres.com/assets/files/meltflow/VAR-Model_Ti-2007-Conference.pdf.
[26] Spitans S, Franz H, Scholz H, Reiter G, Baake E. Magnetohydrodynamics 2017;53:557–69.
[27] Cibula M, Woodside R, King P, Alanko G. Proc Liq Met Process Cast Conf 2017;2017:25–30.
[28] Cibula M, King P, Motley J. Metall Mater Trans B 2020;51:2483–91.
[29] Woodside CR, King PE, Nordlund C. Metall Mater Trans B 2013;44:154–65.
[30] ANSYS fluent 14.5 user's guide. Fluent Inc.; 2012.
[31] Delzant PO, Baque B, Chapelle P, Jardy A. Metall Mater Trans B 2018;49:958–68.
[32] Karimi-Sibaki E, Kharicha A, Wu M, Ludwig A, Bohacek J, Holzgruber H, et al. App. Therm. Eng. 2018;130:1062–9.
[33] Preis K, Bardi I, Biro O, Magele C, Renhart W, Richter KR, et al. IEEE Trans Magn 1991;27:3798–803.
[34] Song H, Ida N. IEEE Trans Magn 1991;27:4012–5.

[35] Kharicha A, Wu M, Ludwig A, Karimi-Sibaki E. Metall Mater Trans B 2016;47:1427–34.
[36] Kharicha A, Wu M, Ludwig A. ISIJ Int 2014;54:1621.
[37] Voller VR, Prakash C. Int J Heat Mass Tran 1987;30:1709–20.
[38] Schneider MC, Beckermann C. Int J Heat Mass Tran 1995;38(18):3455–73.
[39] Chapelle P, Ward RM, Jardy A, Weber V, Bellot JP, Minvielle M. Metall Mater Trans B 2008;40B:254–62.
[40] El Mir H, Jardy A, Bellot JP, Chapelle P, Lasalmonie D, Senevat J. J Mater Process Technol 2010;210(3):564–72.
[41] Karimi-Sibaki E, Kharicha A, Bohacek J, Wu M, Ludwig A. Adv Eng Mater 2016;18:224–30.
[42] Menter FR, Egorov Y. In: AIAA paper 2005-1095; 2005 [Nevada].
[43] Menter FR, Kuntz M, Langtry R. Turb Heat Mass Transfer 2003;4:625–32.
[44] Wang Q, Zhao R, Fafard M, Li B. App Therm Eng 2015;80:178–86.
[45] Liu ZQ, Qi FS, Li BK, Cheung SCP. Int J Multiph Flow 2016;79:190–201.
[46] Hosamani LG. Scholar Archive 1988;263. https://scholararchive.ohsu.edu/concern/etds/1v53jw97x.
[47] Boivineau M, Cagran C, Doytier D, Eyraud V, Nadal M-H, Wilthan B, et al. Int J Thermophys 2006;27:507–29.
[48] Kaschnitz E, Reiter P, McClure JL. Int J Thermophys 2002;23:267–75.
[49] Valencia JJ, Quested PN. ASM International 2008;15:468–81.
[50] Klassen A. Friedrich-alexander-universität. PhD. Thesis. 2018 [Germany].
[51] Karimi-Sibaki E, Kharicha A, Wu M, Ludwig A, Bohacek J. A parametric study of the Vacuum Arc Remelting (VAR) process: effects of arc radius, side-arcing, and gas cooling. Metall Mater Trans B 2020;51:222–35. https://doi.org/10.1007/s11663-019-01719-5.